communications biology

Article

https://doi.org/10.1038/s42003-024-06115-7

Distinct forms of structural plasticity of adult-born interneuron spines in the mouse olfactory bulb induced by different odor learning paradigms

Check for updates

Aymeric Ferreira[1,2], Vlad-Stefan Constantinescu[1,3], Sarah Malvaut[1,3], Armen Saghatelyan[1,3,4] ✉ & Simon V. Hardy[1,2,5] ✉

The morpho-functional properties of neural networks constantly adapt in response to environmental stimuli. The olfactory bulb is particularly prone to constant reshaping of neural networks because of ongoing neurogenesis. It remains unclear whether the complexity of distinct odor-induced learning paradigms and sensory stimulation induces different forms of structural plasticity. In the present study, we automatically reconstructed spines in 3D from confocal images and performed unsupervised clustering based on morphometric features. We show that while sensory deprivation decreased the spine density of adult-born neurons without affecting the morphometric properties of these spines, simple and complex odor learning paradigms triggered distinct forms of structural plasticity. A simple odor learning task affected the morphometric properties of the spines, whereas a complex odor learning task induced changes in spine density. Our work reveals distinct forms of structural plasticity in the olfactory bulb tailored to the complexity of odor-learning paradigms and sensory inputs.

During the early postnatal period, the developing brain is shaped and remodeled in response to environmental stimuli. The major changes that occur during these critical periods of development, which are marked by a high level of plasticity, are activity-dependent structural modifications when some synaptic connections are reinforced and maintained while others are eliminated[1]. This increased level of remodeling in response to environmental stimuli is attenuated in the mature brain when the critical period ends, except for adult neurogenic regions such as the olfactory bulb (OB) and dentate gyrus, which receive new neurons throughout the lifespan of animals[2,3]. The OB is the first relay of olfactory information processing and is an excellent model for studying how various types of structural modifications are triggered in response to environmental stimuli and learning and how these changes allow for the adaptation of bulbar network functioning and animal behavior.

In the OB, the two main populations of interneurons, granule and periglomerular cells (GCs and PGs), are constantly renewed through the process of adult neurogenesis[2]. GCs establish a particular form of connection with the principal cells of the OB, mitral and tufted cells, through reciprocal dendrodendritic synapses. The inhibition of principal cells by GCs is crucial for olfactory information processing and olfactory behavior[2]. In addition to being renewed, GCs also exhibit a high level of structural plasticity that persists after their full morpho-functional maturation[4]. In fact, ~20% of fully mature GC dendritic spines are constantly being added/removed from the OB circuitry[5]. This persistent structural plasticity optimizes odor information processing in the adult OB[5] and is modulated by odor learning[6,7] and sensory activity[8,9]. Indeed, it has been shown that odor learning induces an increase in the spine density of GCs[6,7] while sensory deprivation decreases the spine density[8–10]. Moreover, in vivo imaging studies have revealed that another type of structural plasticity involving the relocation of mature spines allows for the rapid adaptation of the OB circuitry to changes in the olfactory environment[4,5,11]. This process has been shown to be specific to mature adult-born GCs[5,11,12], which are known to play a unique role in OB functioning compared to their early-born counterparts. Notably, during their integration into the OB neuronal network,

[1]CERVO Brain Research Center, Quebec City, QC G1J 2G3, Canada. [2]Department of Biochemistry, Microbiology, and Bioinformatics, Université Laval, Quebec City, QC G1V 0A6, Canada. [3]Department of Psychiatry and Neuroscience, Université Laval, Quebec City, QC G1V 0A6, Canada. [4]Department of Cellular and Molecular Medicine, University of Ottawa, Ottawa, ON K1N 6N5, Canada. [5]Department of Computer Science and Software Engineering, Université Laval, Quebec City, QC G1V 0A6, Canada. ✉e-mail: asaghate@uottawa.ca; simon.hardy@ift.ulaval.ca

two- to three-week-old adult-born OB neurons go through a phase when they are more responsive to new odorants and have broader responsiveness to individual odorants[13,14]. Adult-born GCs also play an important role in a wide range of social and spontaneous olfactory behaviors as well as odor learning and memory[15]. Specifically, these cells play a major role in learning an odor discrimination task[16–18], a task that also induces an increase in the spine density of this population of cells[6,7]. Although all these studies highlight changes in spine density, it remains unclear whether the morphometric parameters of spines also change with the level of olfactory stimuli and/or learning. This is particularly relevant given that the size of a spine head is correlated with the surface of the postsynaptic density (PSD) as well as synaptic strength, whereas both the length and width of a spine neck are linked to postsynaptic potential[19–23].

Historically, dendritic spines have been manually classified into a few groups, such as stubby, mushroom, or thin, based on their morphological features, which helps simplify data interpretation[24,25]. However, clustering, an unsupervised learning technique, has emerged as a promising alternative for the analysis of dendritic spines. Clustering groups of spines based on inherent similarities without predefined categories can reveal unknown spine subtypes of functional or pathological relevance, capture continuous variations in spine morphology, and reduce subjectivity and bias in classification[25–27]. By providing a more nuanced and objective perspective on spine diversity, based on various morphometric parameters, clustering can enhance our understanding of neuronal function and dysfunction and capture how specific properties of spines are affected by sensory inputs and/or learning and memory[28,29]. To assess how sensory activity and odor learning of different complexities affect the structural plasticity of adult-born GCs in the OB, we developed a computational pipeline to extract dendritic spines from confocal images and performed cluster analyses of reconstructed dendritic spines based on distinct morphometric features. We discovered an unexpected diversity of structural plasticity of adult-born GCs in response to the level of sensory activities and odor learning of different complexities. Sensory deprivation decreased spine density without any changes in the morphometric properties of the remaining spines or in spine clusters. Interestingly, while complex odor learning increased spine density without any substantial modifications in the morphometric properties of spines, simple odor learning tasks, on the other hand, did not affect spine density but led to the enlargement of remaining spines. Our data reveal that a distinct mode of structural plasticity might be engaged in adult-born GCs to adapt the functioning of the bulbar network in response to the level of sensory input and complexity of odor learning paradigms.

Results

Go/no-go odor discrimination learning tasks of different complexities lead to distinct changes in the spine density of adult-born GCs

We first investigated the impact of odor learning tasks of different complexity on the structural plasticity of adult-born GCs. Approximately 4 weeks following an injection of a GFP-encoding lentivirus into the rostral migratory stream (RMS) (Fig. 1a), mice were trained on a go/no-go olfactory discrimination task and depending on the complexity of the task, different mixes of odors were presented (Fig. 1a). In the simple version of the task, the mice had to discriminate between two dissimilar odorants: 1% octanal as S+ vs. 1% decanal as S-. Animals from the learner group ($n = 4$ mice) received a water reward if the odor was discriminated correctly. Animals from the control group ($n = 3$ mice) were exposed to the same conditions but received a reward regardless of the odor. The learner group reached the criterion of 80% of correct responses in 5 blocks over the course of 1 day (Fig. 1b) and after only three blocks, the success rate of the learner group was significantly different from that of the control group (Student t-test, $p < 0.001$). Following the learning test, the mice were perfused, and high-resolution confocal images of adult-born GCs were acquired (Fig. 1c). We first quantified the spine density on the distal dendrites of adult-born GCs in the external plexiform layer, the site of contact between GCs and bulbar principal neurons. Our quantification did not reveal any significant difference in spine density between the control and go/no-go simple learning groups (0.55 ± 0.21 spines/µm for the control group, $n = 110$ cells from 3 mice vs. 0.55 ± 0.17 spines/µm for the simple learner group, $n = 111$ cells from 3 mice, $p = 0.82$ Fig. 1d).

Another group of animals was trained with a complex version of the go/no-go task involving very similar odor mixtures: 0.6% limonene(+) and 0.4% limonene(−) as S+ vs. 0.4% limonene(+) and 0.6% limonene(−) as S-. The learner group ($n = 7$ mice) reached the criterion of 80% of correct responses after 22 blocks, while the control group, as expected, never reached this criterion. The difference between the learner and control groups in terms of success rate was highly significant after block 13 (Fig. 1e, significant p values: 0.047, 0.043, 0.002, 0.032, 0.004, 0.003, <0.001 for blocks 9, 14, 17, 18, 20, 21, 22 respectively) Interestingly, the assessment of the spine density of adult-born GCs revealed that, unlike the simple discrimination task, the complex task led to an increase in spine density after training (control group: 0.73 ± 0.19 spines/µm, $n = 97$ cells from 4 mice vs. learner group: 0.84 ± 0.25 spines/µm, $n = 104$ cells from 4 mice, $p = 0.001$ with the Student t-test, Fig. 1f, g). These data suggest that the spine density of GCs is differently affected depending on the complexity of the go/no-go learning task.

We also observed that the spine density of GCs from mice of a control group undergoing the complex go/no-go task was higher than the spine density of cells from the control group undergoing the go/no-go simple task (0.55 ± 0.21 spines/µm vs. 0.73 ± 0.19 spines/µm for the simple and complex go/no-go control groups, respectively, $p < 0.001$ with the Student t-test) (Figs. 1d, e). As the mice in the complex go/no-go control group were exposed to odors in an operant conditioning task for a much longer period of time and encountered odors of a more complex nature, these data suggest that the duration of olfactory stimulation and the complexity of the odors used might affect the spine density of adult-born GCs. These results are in line with previous observations showing that a lack of odor stimulation decreases the spine density of adult-born GCs[11,30].

Odor deprivation decreases the spine density of adult-born GCs

We next investigated the impact of decreased levels of olfactory stimulation on the structural plasticity of adult-born GCs. To do so, 14 days following the injection of a GFP-expressing lentivirus into the RMS, we performed a unilateral nostril occlusion to deprive an OB hemisphere of odor stimulation. We used the contralateral OB hemisphere as a control. Following 14 days of sensory deprivation, we performed a quantitative assessment of the spine density of adult-born GCs. To ensure the effectiveness of the sensory deprivation, we assessed the level of tyrosine hydroxylase (TH) expression, which is known to be regulated in an activity-dependent manner[9], in the glomerular layer of the odor-deprived OB hemisphere compared to the control. We observed a characteristic $55.67 \pm 13.05\%$ decrease in TH expression in the glomerular layer of odor-deprived OB (Fig. 2a), which is in line with previous reports[11,30]. Moreover, and in accordance with previous reports[9,11,30], sensory deprivation resulted in a statistically significant decrease in the spine density of adult-born GCs in the odor-deprived OB hemisphere compared to the control OB hemisphere (control OB: 0.55 ± 0.19 spines/µm, $n = 52$ cells from 3 mice vs. occluded OB: 0.44 ± 0.12 spines/µm, $n = 50$ cells from 3 mice, $p < 0.001$ with an unpaired Student t-test; Fig. 2b, c). Our results showed that the level of sensory activity in the OB influenced the plasticity of adult-born GCs by modulating their spine density.

A pipeline to perform quantitative analyses of 3D-reconstructed dendritic spines from confocal images

Our results show that the spine density of adult-born GCs could be differently affected by odor learning tasks of different complexity and sensory stimulation. However, sensory stimulation and learning may induce changes not only in the number of spines but may also affect the morphometric properties of existing spines. We thus developed a pipeline that starts with the 3D-reconstruction of spines, followed by an assessment of up to 10 distinct morphometric parameters, dimension reduction, and cluster analysis. High resolution confocal images of dendritic spines from animals from the different experimental conditions were first obtained (Fig. 3a).

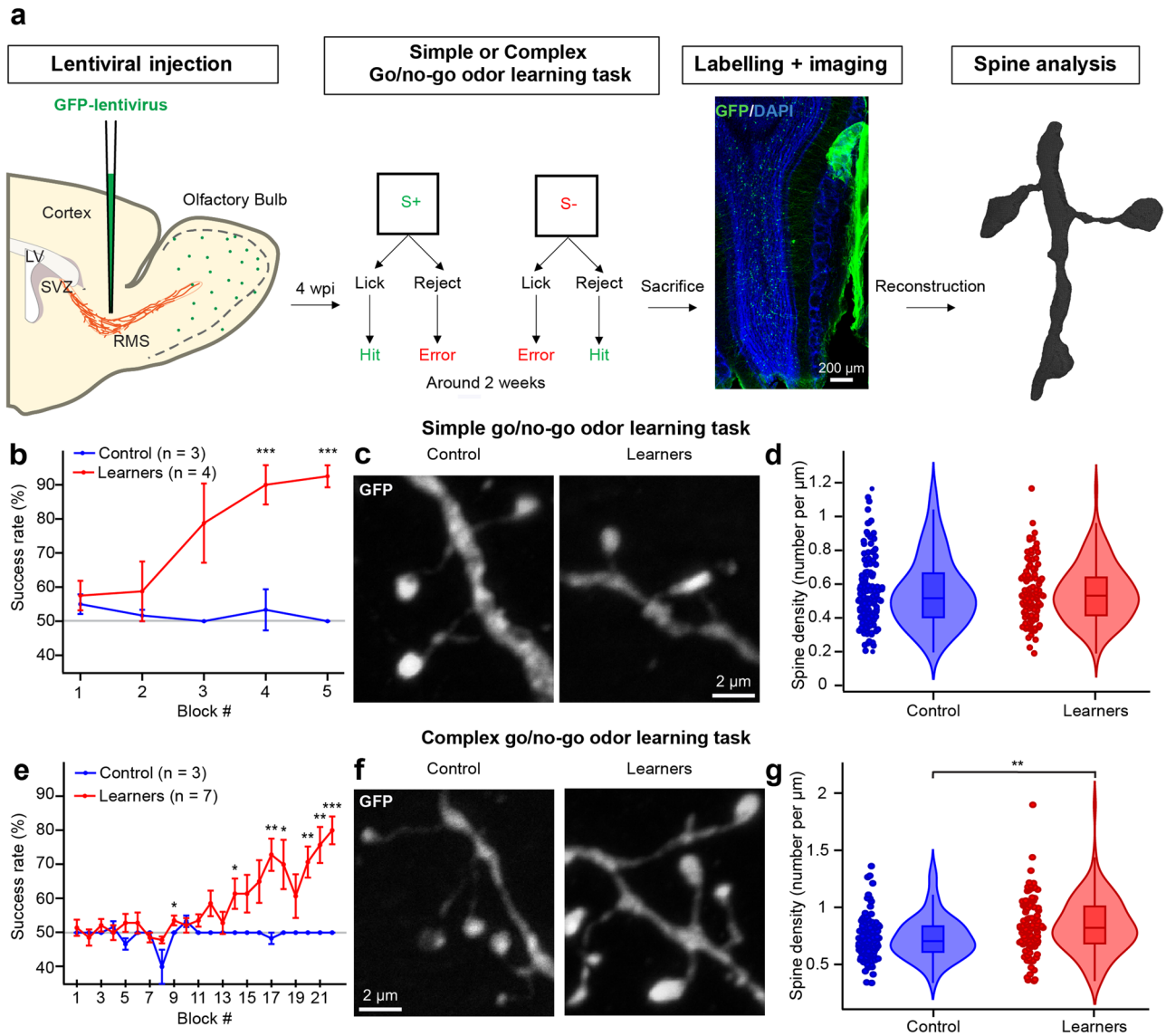

Fig. 1 | Go/no-go odor discrimination affects the spine density of adult-born GCs differently, depending on the complexity of the task. a Timeline of the methods depicting the schematics of the lentiviral injection in the RMS, description of the simple and complex go/no-go odor discrimination task, low magnification image of the OB showing GFP+ adult-born GCs (green), and an example of reconstructed spines. Four weeks after the injection of lentiviruses, the mice began a discrimination task involving different odors. For the simple learning task, an odor composed of 1% octanal was used as the positive stimulus (S+), while 1% decanal served as the negative stimulus (S-). In the complex learning task, the positive stimulus (S+) was a mixture of 0.6% limonene(+) and 0.4% limonene(−), and the negative stimulus (S-) was a mixture of 0.4% limonene(+) and 0.6% limonene(−). A low magnification confocal image of the OB showing GFP+ adult-born GCs (green). The OB section was counterstained with DAPI (blue). The confocal images containing spines were reconstructed into a 3D mesh to assess various morphometric features of spines. **b** Success rate (as a % of total responses) per block for the simple go/no-go task between the control (blue, $n = 3$ mice) and learner (red, $n = 4$ mice) groups, with standard error of the mean for every block. Significant p-values: <0.001 and <0.001 for blocks 4 and 5, respectively. **c** Examples of dendritic spines of adult-born GCs in the control and simple go/no-go learner groups. **d** Following the simple go/no-go task, there were no significant differences in spine density between cells from the control (blue, $n = 110$ cells from 3 mice) and the learner (red, $n = 111$ cells from 3 mice) groups with a box containing the median and whiskers representing the q1 and q3, as well as the lower and upper fence with a p value of 0.23 with an unpaired Student t-test. **e** Percentage of success per block for the complex go/no-go task between the control (blue, $n = 3$ mice) and the learner (red, $n = 7$ mice) groups with standard error of the mean *for every block*. Significant p values with unpaired Student t-test: 0.047, 0.043, 0.002, 0.032, 0.004, 0.003, <0.001 for blocks 9, 14, 17, 18, 20, 21, 22 respectively. **f** Examples of dendritic spines of adult-born GCs in the control and complex go/no-go learner groups. **g** The complex go/no-go task resulted in a significantly higher spine density in the learner group (red, $n = 104$ cells from 4 mice) compared to the control group (blue, $n = 97$ cells from 4 mice) with a box containing the median and whiskers representing the q1 and q3, as well as the lower and upper fence. Significant p-value with unpaired Student t-test: 0.001. *, ** and *** correspond to $p < 0.05$, $p < 0.01$ and $p < 0.001$ with an unpaired Student t-test.

The images were deconvolved using the DAMAS algorithm[31,32], followed by segmentation with the morphological snake Chan-Vese algorithm[33–36]. Lastly, a marching cube algorithm was used to reconstruct the mesh[37,38]. We extracted 4936 spines using the selection tool of Meshlab. For each extracted spine, ten features were calculated: Length, Surface, Volume, Average Distance, Open Angle, Hull Volume, Hull Ratio, Coefficient of Variation in Distance (CVD), Mean Curvature, and Mean Gaussian Curvature (Fig. 3b).

To ensure the integrity of our dendritic spine morphology in the reconstruction process, we conducted a comparative analysis between the spine lengths measured via expert blind assessment and those derived automatically through our reconstruction pipeline. A linear regression analysis yielded a coefficient (R^2) of 0.9477, indicating a robust correlation between the manually measured and the pipeline-calculated lengths. This high degree of correlation suggests that our pipeline does not significantly alter

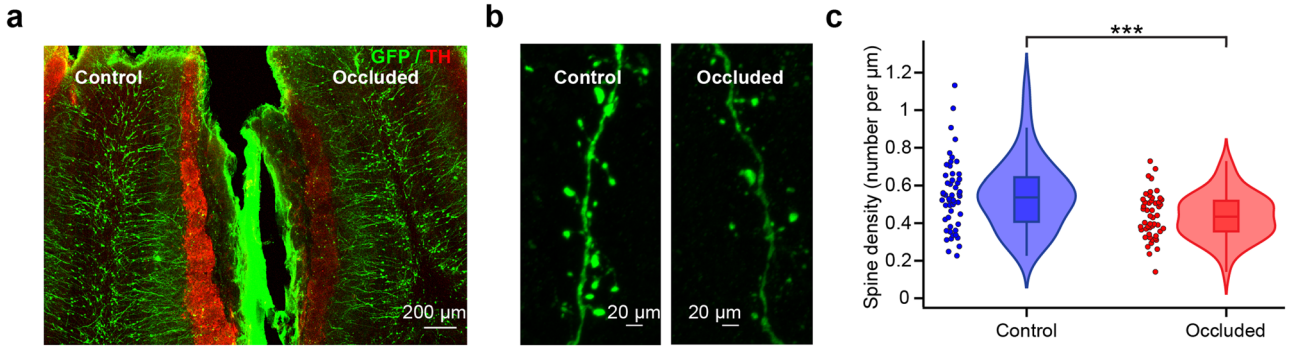

Fig. 2 | Odor deprivation affects the spine density of adult-born GCs. a Confocal image showing two OB hemispheres from an unilateral odor-deprived mouse in which 4-week-old adult-born GCs express GFP (green). Following TH labeling (red), a significant decrease in TH labeling was observed in the occluded OB hemisphere. **b** Representative confocal images of GFP-labeled secondary dendrites of adult-born GCs in both the control and occluded OB hemispheres. **c** Violin plot representation highlighting the significant decrease in the spine density of adult-born GCs following odor deprivation compared to GCs in the control OB (control OB: blue, $n = 52$ cells from 3 mice and odor-deprived OB: red, $n = 50$ cells from 3 mice with a box containing the median and whiskers representing the q1 and q3, as well as the lower and upper fence; $p < 0.001$ with an unpaired Student t-test. *** correspond to $p < 0.001$ with an unpaired Student t-test.

the morphology of the dendritic spines (Supplementary Fig. 1a). A covariance analysis was performed to find the correlation between the features and to only keep the least correlated ones (Supplementary Fig. 1e). Correlations ranging from 0.7 to 0.89 were considered strong, while correlations ranging from 0.9 to 1 were considered very strong based on the literature[39]. A very strong correlation was discovered between Length and Average Distance (0.97). For further analyses, we selected the Length parameter because it is a widely accepted and used feature. The Surface, Volume, and Hull Volume parameters also showed very strong correlations (0.98 between Surface and Volume, 0.97 between Surface and Hull Volume, and 0.99 between Volume and Hull Volume). Of those three parameters, we selected Surface as it is a widely used feature in morphometric assessments of dendritic spines. Lastly, the Hull Ratio, CVD, and Open Angle were retained because they were not correlated with any other feature. We next applied a Standard Scaler followed by a dimension reduction with a Principal Component Analysis (PCA) (Fig. 3c). This led to three Principal Components (PCs) representing 85.4% of the total variance of the data (Supplementary Fig. 1b). Spines from the three experiments were included (go/no-go simple task, go/no-go complex task, and sensory deprivation), together with their respective controls. The resulting representation of the dendritic spines was homogenous, with no obvious clusters (Fig. 3d, e, f). Based on the analysis of the directionality of the coefficients of the linear combination (PCA loadings), PC1 was mostly composed of Surface, Length, and CVD, PC2 was composed of Surface and Open Angle, and, lastly, PC3 was mostly related to the Hull Ratio. The extracted features could then be used for further analyses such as clustering.

Adult-born GC spines can be assembled into different clusters based on experimental conditions

Dendritic spines are highly dynamic, and these protrusions constantly change in size and shape in response to the sensory environment. As there is a continuum of spine shapes and sizes[40], which can also be seen in our dataset after dimension reduction, any attempt to classify spines based on their shape using arbitrary categories could be erroneous[27]. As such, an automatic clustering approach is preferable. In such an approach, the number of clusters is the first parameter that needs to be determined. We identified the appropriate number of clusters for our spine dataset using three different scores: the Elbow score, the Silhouette score, and the Calinski-Harabsz score (Fig. 4a and Supplementary Fig. 1c, d). All three scores suggested that five clusters were present in the dataset. Consequently, we applied a K-Means clustering algorithm with 5 clusters. The result of this algorithm lead to the following clusters. Cluster 1 ($n = 1160$ spines) was located on the low value of the first principal component (mean PC1 = –1.683). Cluster 2 ($n = 790$ spines) was located on the high value of the first principal component (mean PC1 = 2.146). Cluster 3 (n = 628 spines) was located in the middle of the first principal component (mean PC1 = 0.551), but with a high PC2 value (mean=1.866). Cluster 4 (n = 1610 spines) was located at the low value of PC3 (mean = –0.860) and cluster 5 ($n = 748$ spines) was located at the high value of PC3 (mean=1.095) and the low value of PC2 (mean = –1.224) (Fig. 4b). An assessment of the reconstructed spines in each cluster made it possible to associate the mean value of each feature to the morphology of the spine (Fig. 4c). Cluster 1 was mainly composed of small stubby spines or small mushrooms, with a short length (1.39 ± 0.31 µm), small surface area (8.24 ± 4.03 µm^2), small CVD (0.28 ± 0.08), and particularly high Open Angle (0.94 ± 0.11). Cluster 2 was composed of long mushrooms with a long length (3.59 ± 0.81 µm), high CVD (0.45 ± 0.07), and very high surface area (19.35 ± 6.65 µm^2). Cluster 3 was composed of spines with a large surface area (26.17 ± 9.18 µm^2). However, these spines were generally shorter than the spines in cluster 2 (2.55 ± 0.51 µm) and had a higher Open Angle (1.01 ± 0.16). Clusters 4 and 5 had similar spines, with similar lengths (1.89 ± 0.31 µm and 2.07 ± 0.52 µm, respectively), similar surface areas (9.36 ± 4.16 and 8.42 ± 3.88, respectively), similar Open Angles (0.69 ± 0.16 and 0.66 ± 0.17, respectively), and similar CVDs (0.41 ± 0.05 and 0.451 ± 0.05, respectively). However, the spines of cluster 5 were more elongated with higher Hull Ratio (0.85 ± 0.20 vs. 0.40 ± 0.11 for clusters 5 and 4, respectively) which, for these spines, reflect a lower volume as compared to spines of cluster 4. The clustering of dendritic spines of adult-born GCs based on their morphometric features allowed us to determine whether spines from one or several clusters were morphologically altered in response to a simple or complex go/no-go odor learning task and to sensory deprivation.

Sensory deprivation does not affect spine morphology

Our results, as well as those from previous reports[11,30], indicate that sensory deprivation led to a decrease in the spine density of adult-born GCs. It remains unknown, however, whether sensory deprivation also changes the morphometric properties of the remaining spines. To address this issue, we compared the morphometric features of GC spines in the occluded odor-deprived group ($n = 370$ spines) to those of GC spines in the control group ($n = 457$ spines). We observed no significant differences in any of the morphometric properties of GC spines between the odor-deprived and control groups (Fig. 5a). Cohen's term d (effect size index) showed a very small to small effect for every variable. After clustering, no differences in cluster distribution were seen with the Agresti-Caffo test (Fig. 5b). The most prevalent clusters of spines were clusters 4 and 5, which contained similar spines. These spines were relatively small with thin-like spines that represented 50.4% and 56% of the total spines for the control and occluded groups, respectively. Spines with a high surface area (clusters 2 and 3) had a representation of 31.5% and 28.4% for the control and occluded groups, respectively. To ensure that there were no changes in morphologies within

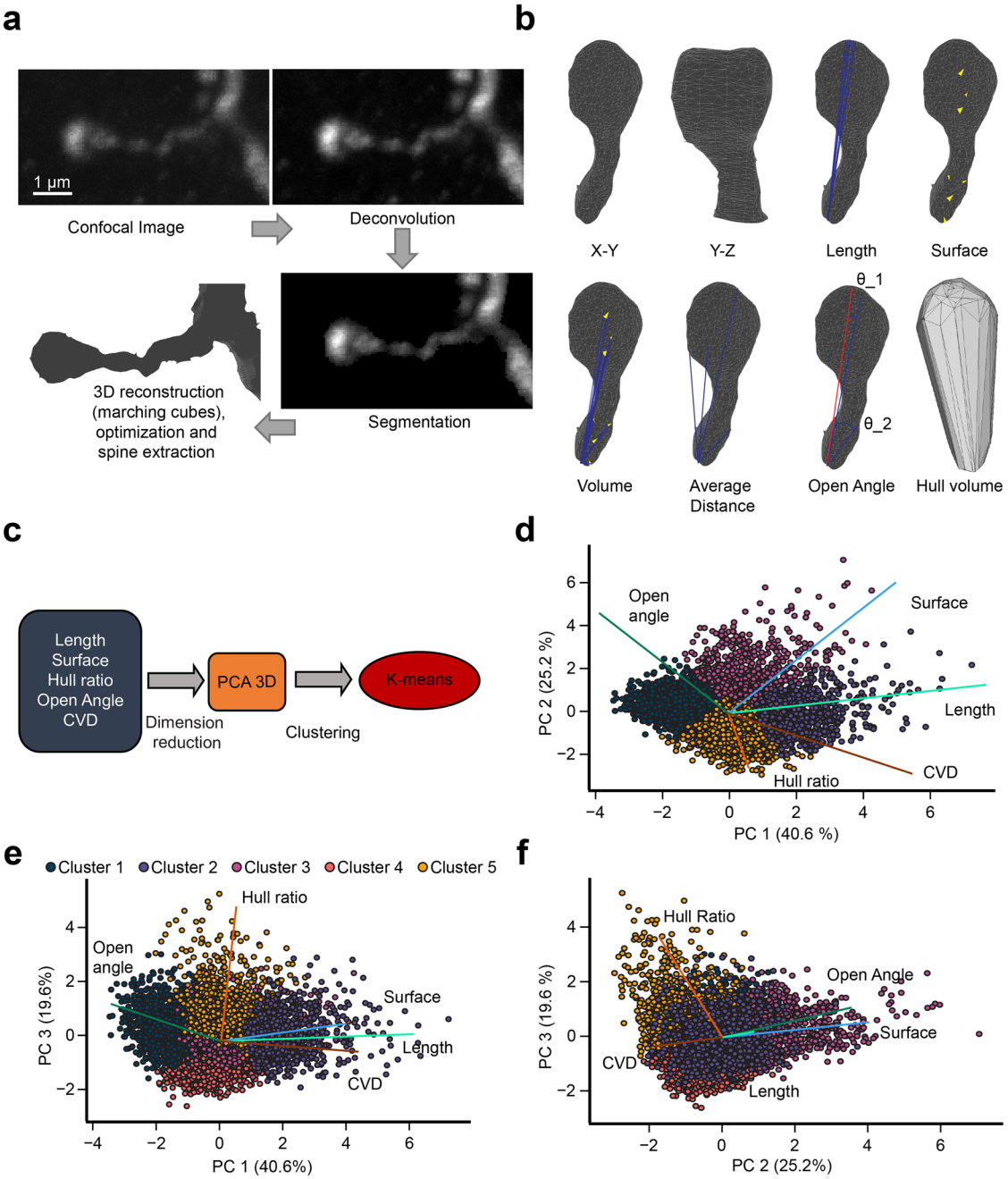

Fig. 3 | Reconstruction of dendritic spines from confocal microscopy images and analysis pipeline. a Confocal image (top left) of a dendritic segment of an adult-born GC with a dendritic spine. The same image after deconvolution (top right), segmentation (bottom right), and reconstruction (bottom left). **b** Different representations of a dendritic spine reconstructed in 3D with calculated morphometric features. **c** General pipeline to analyze dendritic spines based on a combination of dimension reduction and statistical methods. **d**–**f** Biplot representation of all reconstructed spines after PCA, where each point represents a dendritic spine and is color-coded based on cluster identity obtained after K-Means. Each line represents the directionality of the coefficients of the linear combination (PCA loadings) for each feature.

the cluster, we compared the occluded and control groups for each cluster. No differences were seen in spine morphologies for any cluster (Fig. 5c). This result suggests that sensory deprivation via nostril occlusion only affected the spine density of adult-born GCs, with no changes in the morphometric properties of the remaining spines.

Different types of plasticity are evoked by learning, depending on the complexity of the go/no-go task

Given the distinct effect on spine density of adult-born GCs in the control groups of go/no-go simple and complex odor learning tasks, we determined whether the complexity of the operant task also influenced the morphology of dendritic spines. We compared spines from both the simple ($n = 1334$ spines) and complex task ($n = 832$ spines) control groups. Interestingly, we observed major differences between spines from both control groups. Cohen's term' size effect test reported a very small to small effect for every variable. When both control groups were compared, significant differences were found with respect to spine surfaces ($13.37 \pm 8.90\ \mu m^2$ vs. $10.95 \pm 7.16\ \mu m^2$ for the simple and complex task control groups, respectively; $p < 0.001$ with the Student t-test), Hull Ratio (simple task control group: 0.60 ± 0.21 vs. 0.50 ± 0.19 for the simple and complex task control groups, respectively; $p < 0.001$ with the Student t-test), CVD (0.41 ± 0.09 vs. 0.36 ± 0.09 for the simple and complex task control groups, respectively;

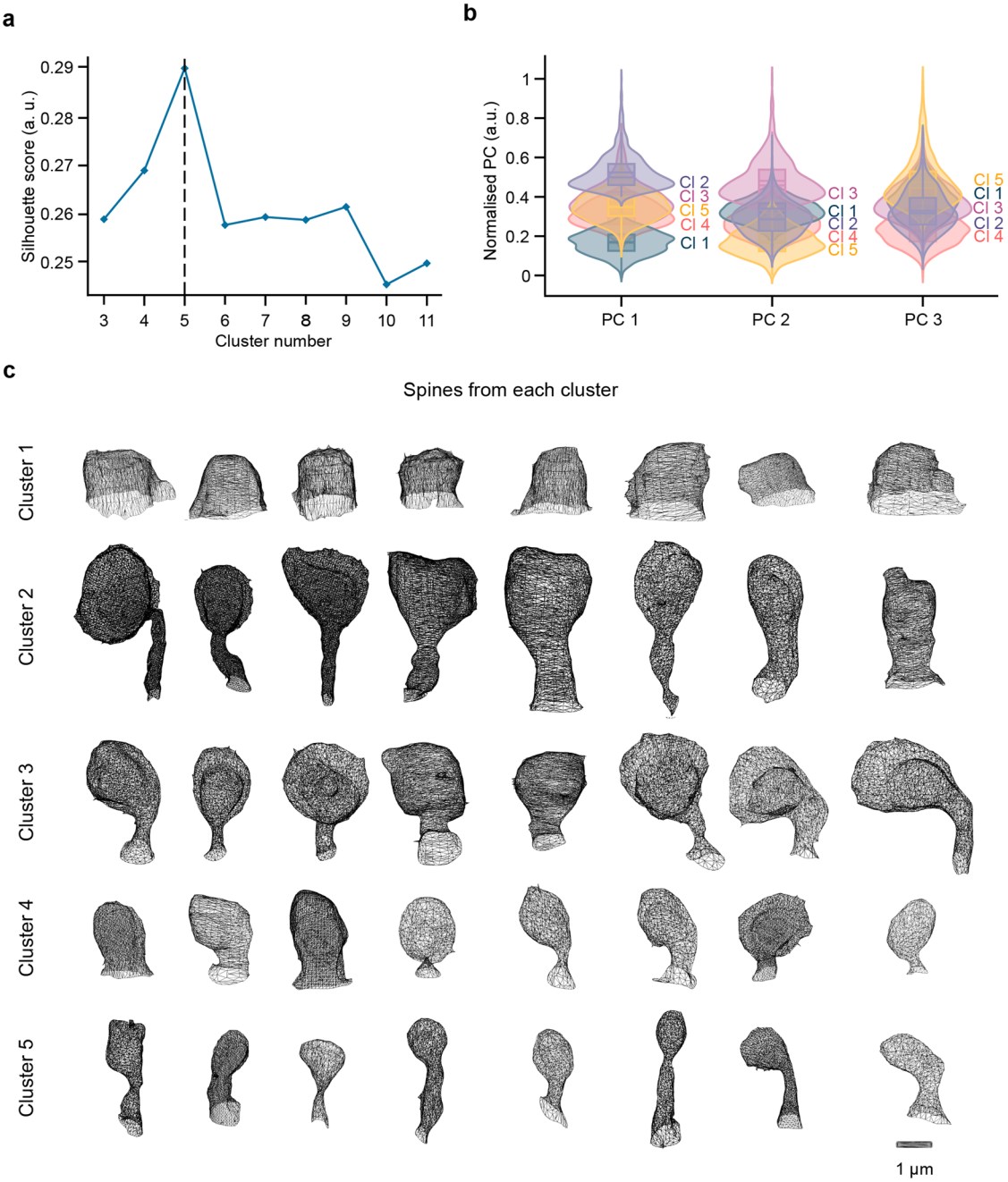

Fig. 4 | Clustering of spines of adult-born GCs based on their morphological features. a Representation of the silhouette score for 3 to 11 clusters. The dashed line shows the optimal number of clusters. **b** Violin plot representation of each principal component (PC) after normalization for five clusters with a box containing the median and whiskers representing the q1 and q3, as well as the lower and upper fence. **c** Morphological representation of ten reconstructed spines for each of the five clusters taken near the center of each cluster.

$p < 0.001$ with the Student *t*-test), and Open Angle (0.85 ± 0.19 vs. 0.64 ± 0.19 for the simple and complex task control groups, respectively; $p < 0.001$ with the Student *t*-test, Supplementary Fig. 2a). No difference was observed with respect to spine length. The cluster distribution between the two control groups was also different. There were significantly more spines with cluster 2 (Agresti-Caffo, $p < 0.001$) and cluster 4 (Agresti-Caffo, $p < 0.001$) in the control group of the complex go/no-go task, which concomitantly resulted in fewer spines with a cluster 3 morphology (Agresti-Caffo, $p < 0.001$) and a cluster 5 morphology (Agresti-Caffo, $p < 0.001$) (Supplementary Fig. 2b). The KDE map shows that the distribution of the spine morphology remains consistent between the two control groups (Supplementary Fig. 2c). The duration of the odor stimulation in the go/no-go task and the complexity of the odor used thus had an impact on the morphology of the dendritic spines, even when no association between a particular odorant and a reward was involved.

We next determined whether learning a go/no-go simple task that did not induce any changes in the spine density of adult-born GCs affected the morphometric properties of spines. The morphometric properties of spines from the learner group of the simple go/no-go task ($n = 767$ spines from 111 cells, 3 mice) were compared to those of the control group ($n = 1334$ spines from 119 cells, 3 mice). Cohen's term *d* was calculated and indicated a very small to small effect for every variable. Significant differences (Fig. 6a) were found for four features between the control and learner groups: Surface, with 13.37 ± 9.0 µm^2 and 16.19 ± 10.40 µm^2 ($p < 0.001$ with

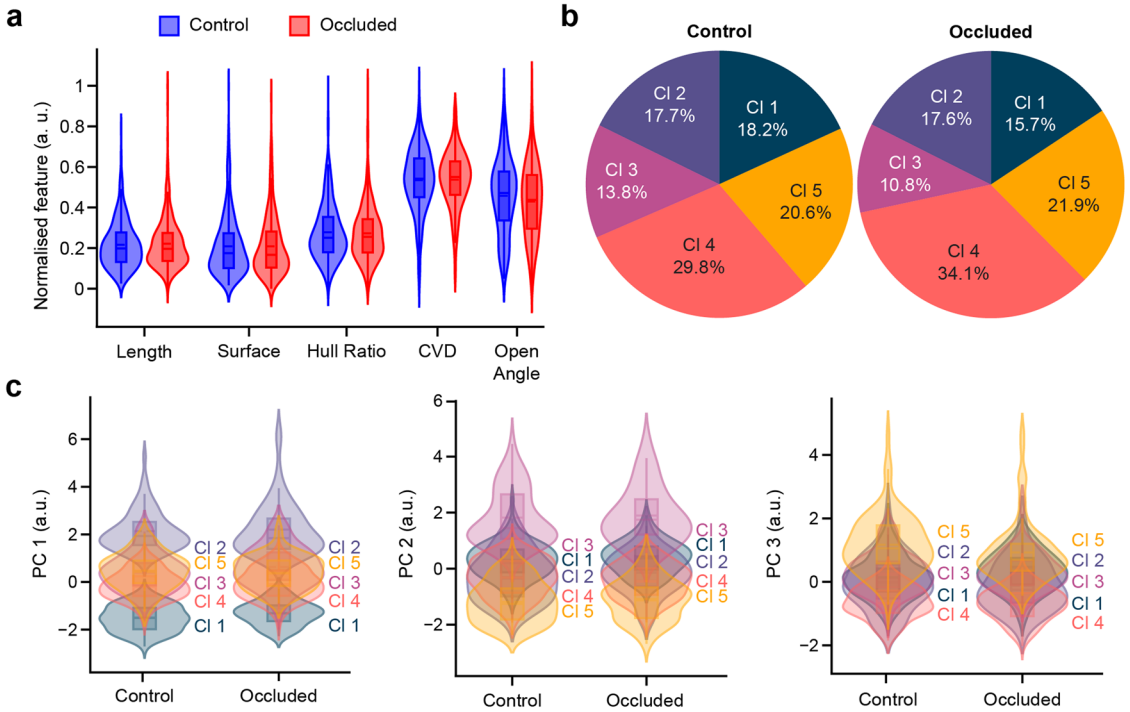

Fig. 5 | Sensory deprivation does not affect dendritic spine morphologies. a Violin plot representation of spines from the control (blue) and occluded (red) groups for each normalized feature with a box containing the median and whiskers representing the q1 and q3, as well as the lower and upper fence. **b** Pie chart representation of the cluster distributions in the control and occluded groups. **c** Violin plot representation of each principal component after dimension reduction and normalization for five clusters for the control and occluded groups with a box containing the median and whiskers representing the q1 and q3, as well as the lower and upper fence.

the Student *t*-test) for the control and learner groups, respectively, Hull Ratio, with 0.6 ± 0.21 and 0.57 ± 0.20 ($p = 0.005$ with the Student *t*-test) for the control and learner groups, respectively, CVD, with 0.41 ± 0.09 and 0.4 ± 0.09 ($p = 0.001$ with the Student *t*-test) for the control and learner groups, respectively, and Open Angle, with 0.85 ± 0.19 and 0.93 ± 0.18 ($p < 0.001$ with the Student *t*-test) for the control and learner groups, respectively. No significant changes were observed in spine length between the two groups. These results indicate that while spine length was not affected by the simple go/no-go learning task, this learning paradigm led to larger spines, as attested to by changes in the Surface, Hull Ratio, CVD, and Open Angle.

The changes in morphology were also significant with respect to the distribution of several clusters (Fig. 6b). Following learning, the proportion of spines in cluster 2 decreased from 14.6% in the control group to 8.74% in the learner group (Agresti-Caffo, $p < 0.001$). Similarly, the spines of cluster 5 decreased from 17.9% in the control group to 14% in the learner group (Agresti-Caffo, $p = 0.017$). The proportion of spines in cluster 3 increased from 17.7% in the control group to 31% in the learner group (Agresti-Caffo, $p < 0.001$). Overall, learning to associate the simple odor with a water reward in go/no-go odor discrimination task led to the appearance of more spines with a mushroom-like shape as seen by an increase in the Surface and Open Angle and a reduction in the Hull Ratio and CVD. To ascertain that each cluster in both groups were represented by spines of similar morphologies, the spines of each cluster in the control group were compared to those of the learner go/no-go group. No differences were seen in spine morphologies within any cluster (Fig. 6c). To understand the morphological changes between clusters, Kernel Density Estimation (KDE) was used to map the spine densities of clusters 2, 5, and 3 as well as PC1 and PC2 (Fig. 6d). After learning, spines from cluster 2, which are represented by long mushrooms, and spines from cluster 5, which are represented by thin spines with complex structures, tended to move toward cluster 3. These observations thus implied that spines from clusters 2 and 5, but not spines from clusters 1 and 4, tended to change their morphology toward that of spines from cluster 3, i.e., mushroom-like spines with large surfaces.

As complex go/no-go odor discrimination tasks resulted in an increase in spine density (Fig. 1g), we next determined whether this task also induced changes in spine morphology. The control group ($n = 832$ spines from 99 cells, 4 mice) was compared to the learner group ($n = 1175$ spines from 112 cells, 4 mice) that performed the complex go/no-go task. Interestingly, no significant differences (Fig. 7a) were found for any of the morphometric features. Cohen's term *d* reported a very small to small effect for every variable. We observed only a slight change in the distribution of clusters (Fig. 7b) with the population of cluster 5 increasing (Agresti-Caffo, $p = 0.020$) between the control (9.38%) and the learner (12.7%) groups. The spines in cluster 3, which are mushroom-like spines with large surface areas, were particularly underrepresented, with only 2.52% and 2.55% in the control and learner groups, respectively. However, cluster 4, which contains thin spines with no complex shapes, constituted 42.5% of the control group and 41.1% of the learner group. To ascertain whether the clusters were represented by spines with the same morphologies, we compared the control and learner go/no-go groups for each cluster. No differences were observed in spine morphologies within any cluster (Fig. 7c). To understand the changes in morphologies, KDE maps of spine densities for clusters 2, 3, and 5 were computed (Fig. 7d). The differences in the distribution of spines in cluster 3 and cluster 2 were not significant between the control and learner groups. There were significant differences between the control and learner groups for the spines in cluster 5 that tended to change their morphology in the opposite direction to cluster 3, which could explain the low representation of spines in cluster 3 and the high number of spines with a cluster 5 morphology. This is in contrast to the changes observed in the simple go/no learning task when the spines belonging to cluster 5 tended towards cluster 3.

Overall, our data indicate that, depending on the level of sensory stimulation and the complexity of the odor learning paradigms, distinct forms of structural plasticity of adult-born GCs might be involved in adapting the

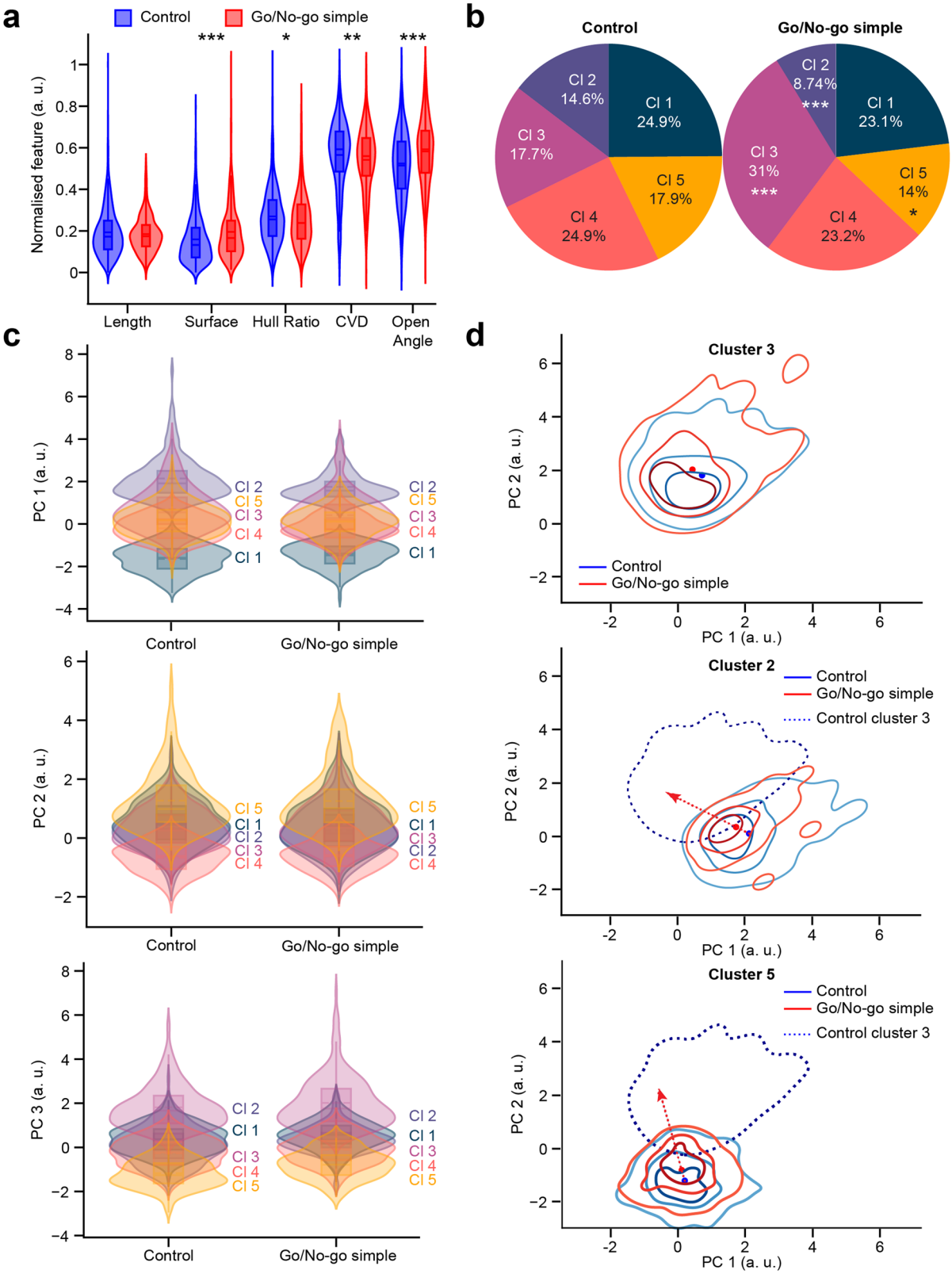

Fig. 6 | A simple go/no-go task leads to changes in spine morphology. a Violin plot representation of each normalized morphometric feature for the control (blue) and learner (red) groups. With unpaired Student *t*-test, *p* values: 0.09, <0.001, 0.005, 0.001, <0.001 for Length, Surface, Hull ratio, CVD, and Open angle, respectively. **b** Pie chart representation of the cluster distribution in the control and go/no-go learner groups performing a simple odor discrimination task. Note the decrease in the representation of clusters 2 and 5, as well as the increase in cluster 3 following learning. With Agresti-Caffo independence test: 0.36, <0.001, <0.001, 0.38, 0.02 for Clusters 1, 2, 3, 4, and 5, respectively. **c** Violin plot representation of the five clusters after dimension reduction and for each normalized PC for the control and learner groups. **d** KDE map of the representation of the spine densities of clusters 3, 2, and 5 in the space of PCs 1 and 2 for the control group in blue and the learner group in red. The dotted line corresponds to the KDE representation of the spine density of cluster 3. The red arrow represents the direction of the cluster from the center of the KDE map for the control group to the center of the KDE map for the go/no-go simple group. *, ** and *** correspond to $p < 0.05$, $p < 0.01$ and $p < 0.001$ with an unpaired Student *t*-test.

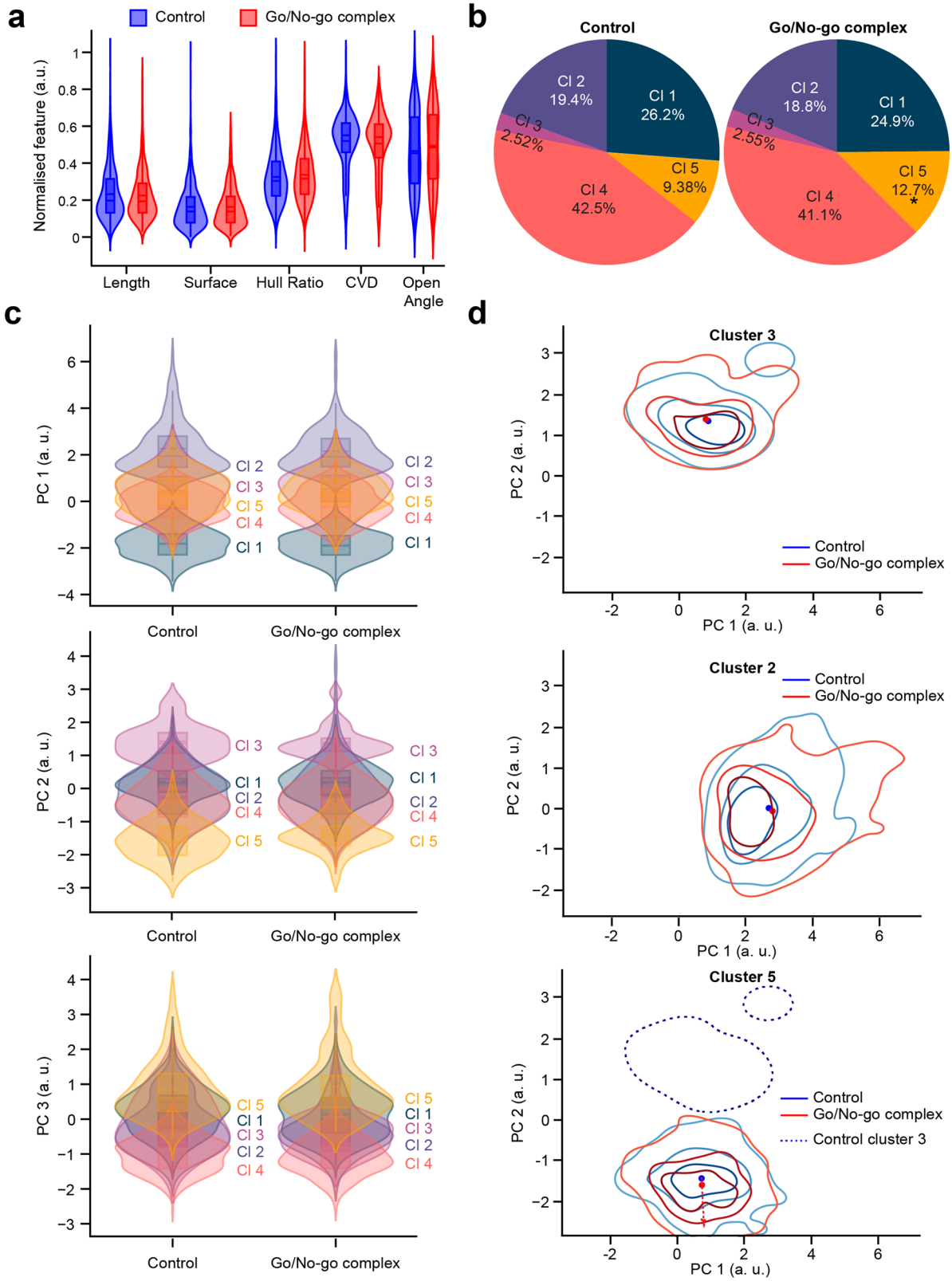

functioning of the bulbar network. Sensory deprivation decreased spine density, with no changes in spine morphology. The simple go/no-go odor learning task led to changes in the morphometric properties of existing spines without any modifications in spine density. On the other hand, the complex go/no-go learning task increased spine density, with only subtle changes in the morphometric properties of spines. The present study thus shows that there was a vast panoply of distinct forms of structural modifications in the bulbar network.

Discussion

In the present work we show that the spines of adult-born GCs exhibited different modes of structural plasticity in response to the level of sensory

Fig. 7 | Complex go/no-go odor learning does not lead to changes in spine morphology. a Violin plot representation of the control group in blue and the learner group in red for Length, Surface, Hull Ratio, CVD, and Open Angle after normalization for the morphometric features with a box containing the median and whiskers representing the q1 and q3, as well as the lower and upper fence. With an unpaired Student *t*-test, *p* values: 0.15, 0.79, 0.09, 0.78, 0.45 for Length, Surface, Hull ratio, CVD and Open angle, respectively. **b** Pie chart representation of the cluster distribution in the control and learner groups. With Agresti-Caffo independence test: 0.49, 0.75, 0.99, 0.52, 0.02 for Clusters 1, 2, 3, 4, and 5, respectively. **c** Violin plot representation of each PC after dimension reduction and normalization for five clusters for the control and learner groups with a box containing the median and whiskers representing the q1 and q3, as well as the lower and upper fence. **d** KDE map of the representation of the spine density for clusters 3, 2, and 5 in the space of PC1 and PC2 for the control group in blue and the learner group in red. The dotted line corresponds to the KDE representation of the spine density of cluster 3. The red arrow represents the direction of the cluster from the center of the KDE map for the control group to the center of the KDE map for the go/no-go simple group.

activity and the complexities of odor learning tasks. The computational pipeline we developed enabled us to divide the reconstructed spines into five distinct clusters based on various morphometric properties and to assess how the level of sensory stimulation or odor learning affected the morphology and type of spines. The analysis of the cluster distribution of spines from various conditions together with the comparison of KDE maps highlighted the spines movement dynamics over the landscape of their shapes induced, or not, by olfactory stimulation and learning. We show that sensory deprivation led to a uniform reduction in spine density, with no changes in the morphology of the spines or their distribution in the different clusters. The difficulty of a go/no-go odor learning task determined whether the structural plasticity of adult-born GCs was reflected by changes in the morphometric properties of the spines or spine density. In fact, while a simple odor discrimination task affected the morphology of the spines, the complex odor learning task resulted in a higher spine density, with no substantial differences in the clusters distribution.

Why are such distinct types of structural plasticity of adult-born GCs engaged in response to the level of sensory input and the complexity of odor learning tasks? While further work is required to understand what the functional properties of each spine cluster of adult-born GCs are and how each cluster is involved in odor information processing, it is conceivable that the type of structural plasticity of adult-born GCs is tailored to the needs of the bulbar network in order to adjust its functioning to changing environmental conditions and learned experiences. Sensory deprivation led to an overall reduction in spine density. While these data are consistent with previous reports[11,30], it was unknown how the morphometric properties of the remaining spines are affected. Our computational pipeline and clustering analysis show that sensory deprivation did not lead to any changes in the morphometric properties of spines and the clusters. GCs synchronize the activities of principal OB neurons through their dendro-dendritic reciprocal synapses, which allows odor information to be processed in the bulbar network[41,42]. Adult-born neurons may synchronize the activities of new assemblies of principal neurons involved in new memory[16,43–45]. The global reduction in odor-induced activity through unilateral nostril occlusion may not require the synchronization of new assemblies of principal cells because of the lack of sensory inputs. The OB operational neuronal network may thus be maintained through other mechanisms, with no additional structural plasticity required by GC spines. Indeed, it has been shown that sensory deprivation affects not only the output synapses of GCs, as evidenced by the decrease in spine density, but also induces an increase in the input synapses onto GCs[10]. Furthermore, sensory deprivation also triggers an increase in the excitability of newborn GCs, leading to an increase in action potential-dependent GABA release and unaltered synchronized activity of principal cells[46]. These studies highlight the adaptive responses in the OB network and indicate that increases in excitability and input synapses onto adult-born GCs maintain the functioning of the neuronal network with no additional need for changes in the morphometric properties of GC spines.

On the other hand, depending on the complexity of the olfactory learning task, the structural plasticity of adult-born GCs is manifested either by changes in the morphometric properties of spines and/or by increases in spine density. The simple go/no-go odor task depended on the presentation of two distinct odors that mice were able to learn very quickly, i.e., in 5 blocks over the course of 1 day. This contrasts with the complex go/no-go learning task based on discrimination between two very similar odor mixtures, which took the mice 22 blocks over multiple days to learn. Our data suggest that learning a simple odor discrimination task might be achieved by enlarging the pre-existing spines of adult-born GCs without forming new ones. In contrast, the complex odor discrimination task required the formation and stabilization of additional spines of adult-born GCs that might be necessary for synchronizing the activities of new principal cell assemblies. These data are in line with previous reports showing that there is an increase in the spine density of adult-born but not pre-existing GCs during a complex odor learning task[6,7]. Interestingly, this increase is driven by inputs from the piriform cortex[6,7]. Optogenetic stimulation of these projections strengthens learning-induced plasticity[7], while their inactivation impedes learning-induced changes[6]. It remains largely unknown how a simple odor learning task affects the feedback projections onto the OB and whether the changes in spine morphologies observed during this task are driven locally in the bulbar network or are mediated by centrifugal projections from other brain regions. It is conceivable that, depending on the complexity of the odor learning task, distinct brain regions or different levels of feedback are required to associate the water reward with odor stimuli and trigger distinct types of structural plasticity. In line with this, it has been shown that different types of odor-associative learning tasks may induce distinct patterns of early immediate gene expression in the orbital and infralimbic cortices[47], which are known to be involved in odor memory[48]. Future experiments based on mapping the activated neuronal assemblies across the brain regions during simple and complex go/no-go odor learning tasks will be required to address this issue.

The reconstruction of dendritic spines in three dimensions made it possible to obtain more morphometric information than analyses of 2D images of spines. The most relevant features were Length, Surface, Hull Ratio, CVD, and Open Angle, followed by PCA, which reduced the number of dimensions. As spine shapes form a continuum and cannot be categorized[49], the clustering was performed on dendritic spines based on different morphometric properties. When the spines in each cluster were examined, a general characteristic for each cluster could be determined. Cluster 1 predominantly consisted of small stubby spines, cluster 2 of long mushroom spines, cluster 3 of mushroom spines with a larger surface area, and clusters 4 and 5 of long thin spines distinguished by a higher Hull Ratio for cluster 5. The Open Angle appeared to be a highly effective indicator for distinguishing between mushroom and stubby spines, with the mean value being larger for the stubby spines. The CVD was particularly high for mushroom spines because of their distinct morphology, which is comprised of a head and a neck. The Hull Ratio represents elongated spines with a lower volume. Although all these parameters allowed us to cluster spines based on their morphometric properties, our KDE map representation of spine clusters also made it possible to highlight clusters that were particularly sensitive to odor learning and, at the same time, determine the transition of clusters from one to another within their continuum. Spines in cluster 1 were particularly stable and did not undergo any modifications in response to sensory deprivation or to a simple or complex odor learning task. This contrasts with spines in the other clusters that were modified by learning to different degrees. Although the simple odor learning task induced changes in clusters 2, 3, and 5, the KDE map representation shows that spines in clusters 2 and 5 changed their morphology toward the morphology of spines in cluster 3. Clusters 2 and 5 consisted of mushroom spines with smaller surface areas and long thin spines, respectively, whereas cluster 3 harbored mushroom spines with a larger surface area. The transition of clusters 2 and 5 to cluster 3 indicated that these spines became

bigger in response to a simple go/no-go odor learning task. The larger spines are usually associated with a larger PSD, which might lead to increased synaptic efficacy. It should be mentioned, however, that the spines of GCs are constituents of dendro-dendritic reciprocal synapses, which implies that the same spine contains post-synaptic glutamatergic and pre-synaptic GABAergic parts. It is currently unclear whether the increased surface area reflects changes in both the pre- and post-synaptic constituents and what functional outcome is induced by these changes.

Interestingly, while the complex odor learning task largely resulted in changes in spine density, the subtle morphometric modifications observed after this learning task were opposite to those of the simple go/no-go task. Our cluster analysis and KDE map representation show that there was an increase in spines in cluster 5 while the spines in the cluster 3 were particularly under-represented in both the control (2.52%) and learner (2.55%) groups. The spines in cluster 5 tended to change their morphology in a direction opposite to cluster 3, unlike with the simple go/no-go learning task where they changed their morphology toward cluster 3. As the complex go/no-go odor learning task led to an increase in spine density, this might reflect the addition of new spines. If this is the case, it would indicate that a complex odor learning task leads to the formation and stabilization of new spines that predominantly belong to cluster 5. On the other hand, sensory deprivation decreased spine density with no noticeable changes in the spine clusters, indicating that the decrease was rather homogenous across the various clusters. At the first sight, the homogenous decrease in the density of spines across the various clusters seem at odds with our previous results showing that spines with spine head filopodia-like protrusions (SHF) are selectively preserved after sensory deprivation[11]. This can be explained by the fact that, first, SHF are very motile and appear and disappear very rapidly within a few minutes[11]. They can be easily observed in time-lapse imaging studies. However, due to their rapid dynamics, they are under-represented in the fixed tissue that we used for our current analysis. Second, SHF were also very thin and were more difficult to reconstruct with our pipeline. Future studies to perform 3D reconstruction and clustering analyses of spines derived from in vivo two-photon imaging studies in the OB, as we did previously[11], combined with further improvements to the 3D reconstruction pipeline, will help address this issue.

In addition to learning-induced changes in the morphometric properties of spines and/or their density, our observations of marked changes in the morphology of the spines of the two control groups performing simple and complex tasks without associating the odor with a water reward (i.e., learning) were intriguing. Almost all the clusters, except cluster 1, were affected. Clusters exhibiting larger changes included cluster 3, which decreased from 17.7% following the simple odor task to 2.17% following the complex go/no-go task, and cluster 4, which showed opposite changes (24.5% following the simple odor go/no-go task vs. 42.5% following the complex go/no-go task). The almost complete disappearance of cluster 3, which was central to the simple odor learning-induced changes, following the go/no-go complex task highlighted once again the different levels of structural modification of adult-born GCs in response to environmental challenges. This also indicates that the structural plasticity of adult-born GCs might be triggered not only in response to odor learning but also in response to the difficulty of the operating task, the duration of the odor stimulation, or the complexity of the odor mixtures. Future studies to test the role of passive exposure of mice to complex odor mixtures without exposing them to the go/no-go operational task will help resolve these issues.

One of the limitations of our study was that we tailored our 3D reconstruction and computational pipeline to confocal images. We selected this approach given that confocal microscopy is widely used and enables the rapid testing and adaptation of our pipeline to user-specific needs. However, confocal microscopy does not provide sufficient resolution to resolve intricate details of spine morphology. Super-resolution microscopy, such as stimulated emission depletion (STED) microscopy, has recently shown that only a few, if any, stubby spines can be observed in organotypic slices of the hippocampus[23]. It is thus possible that because of lower resolution of confocal microscopy as compared to STED, both small stubby and small mushroom spines were regrouped in the cluster 1 using our analytical pipeline. It should be mentioned, however, that independent of the type of spines in cluster 1, our clustering analysis based on various morphometric properties, automatically derived from the reconstructed dendritic spines without imposing any specific criteria related to the spine's neck or head, showed that all the spines in this cluster had distinctive characteristics compared to the other clusters.

Another limitation of our study was the lack of functional and ultrastructural signatures of clustered spines. Future studies using electron microscopic analyses of spines in a particular cluster and a functional assessment of their properties by combined glutamate uncaging and Ca^{2+} imaging will provide a better understanding of the functions of the spines in each specific cluster and how they are involved in the functioning of the bulbar network.

Lastly, it should be noted that GCs are a very heterogenous population of neurons that are characterized by the expression of distinct neurochemical markers and spatio-temporal assignments in the bulbar network[12,50,51]. Each GC subtype may be involved in a different odor behavior[51]. In the present study, we did not determine whether learning or sensory stimulation-associated changes in spine density and morphometric properties were linked to specific neurochemical signatures of adult-born GCs. Future studies that combine genetic targeting of different subtypes of adult-born GCs and computational assessments of learning-induced morphometric changes in spines will help address these issues.

Although all these limitations will pave the way path for future studies that will broaden our understanding of the structuro-functional properties of spines, the present study revealed that there is a vast panoply of distinct types of structural plasticity in adult-born GCs that are tailored in response to environmental stimuli and learning experiences.

Methods

Animals

Adult (>2-month-old) male C57BL/6 mice (Charles River) were used for all experiments. The experiments were performed in accordance with Canadian Guide for the Care and Use of Laboratory Animals guidelines and were approved by the Animal Protection Committee of Université Laval. The mice were kept in groups of 4–5 on a 12-h light/dark cycle in a temperature-controlled facility (22 °C), with food and water ad libitum. The animals that underwent the go/no-go odor discrimination procedure were partially water-deprived, individually housed, and kept on a reverse light-dark cycle for 7–10 days before beginning the experiments. Animals were randomly assigned to the various experimental groups.

Stereotaxic surgeries

We used a GFP-expressing lentiviral vector (LV-EF1α-puro, SignaGen Laboratories, SL100269) to label neuronal precursors and image GC dendritic spines. Mice were stereotaxically injected in the RMS under isoflurane anesthesia (2–2.5% isoflurane, 1 L/min of oxygen) and were kept on a heating pad during the entire surgical procedure. The following coordinates (with respect to the bregma) were used to target the RMS: anterior-posterior (AP) 2.55, medio-lateral (ML) 0.82, and dorso-ventral (DV) 3.15. The mice were allowed to recover on a heating blanket in a clean cage before returning to the housing room.

Sensory deprivation

Two weeks after the viral injections, a group of animals was unilaterally sensory deprived. Occlusion tubes were made using polyethylene tubing (PE50, I.D. 0.58 mm, O.D. 0.965 mm; Becton Dickinson), with the center blocked using a tight-fitting Vicryl suture knot (3–0; Johnson & Johnson). The 5-mm-long petroleum jelly-coated plugs were inserted in the left nostril of the mice under isoflurane anesthesia, according to the procedure described previously[11,52,53]. The mice were sacrificed by intracardiac perfusion 14 days later (i.e., 4 weeks post-viral injection).

Go/no-go olfactory discrimination learning

Approximately 4–5 weeks after the injection of the GFP-expressing lentivirus, the mice were partially water-deprived to reach 80–85% of their initial body weight prior to starting the go/no-go training. They first underwent training sessions to habituate themselves to the olfactometer chamber and learn how to get a water reward. The mice were trained using 20 trials, with no exposure to an odor, to insert their snouts into the odor sampling port and lick the water port to receive a 3-µL water reward. The two ports were located side-by-side. The reward-associated odor (S+) was then introduced. Inserting the snout into the odor sampling port broke a light beam and opened an odor valve. The duration of the opening was increased gradually from 0.1 to 1 s over several sessions, and mice with a minimum sampling time of 50 ms were given a water reward. The mice usually completed this training after one or two 30 min sessions. Once they had successfully completed this training step, they were subjected to the go/no-go odor discrimination test. Prior to being introduced to the non-reinforced odor (S-), the mice underwent an introductory S- session consisting of exposure to S + for 30 trials. If the success rate was at least 80%, the discrimination task was begun. The mice were then exposed randomly to S+ or S-, and the percentage of correct responses was calculated for each block of 20 trials. If a mouse licked the water port after being exposed to S+ (hit) and did not lick the water port after being exposed to S- (correct rejection), this was recorded as a correct response. A false response was recorded if the mouse licked the water port after being exposed to S- or if it did not lick the water port after being exposed to S+. A mouse was considered successful if it reached a criterion score of 80%. The control group underwent the same go/no-go procedure but received the water reward independently of the odor used (S + or S-). Mice from both groups underwent one of the two versions of the task.

The simple task involved 0.1% octanal (Sigma Aldrich) diluted in 99.9% mineral oil (Sigma Aldrich) as S+ and 0.1% decanal as S-. The complex version of the task involved two mixtures of similar odorants: 0.6% (+)-limonene (Sigma Aldrich) + 0.4% (−)-limonene (Sigma Aldrich) (S+) diluted in 99.9% mineral oil vs. 0.4% (+)-limonene, + 0.6% (−)-limonene (S−) diluted in 99.9% mineral oil. The mice from the two groups were sacrificed by intracardiac perfusion 1 h after completing the task.

Immunohistochemistry

The mice were deeply anesthetized using an intraperitoneal injection of sodium pentobarbital (12 mg/mL; 0.1 mL per 10 g of body weight) and were intracardially perfused with 0.9% NaCl followed by 4% paraformaldehyde (PFA). The brains were collected and were post-fixed overnight in 4% PFA. Horizontal 100-µm-thick OB sections were cut using a vibratome (Leica) and were incubated overnight with a chicken anti-GFP primary antibody (Aves Labs, GFP-1020, 1:1000) diluted in 1% PBS supplemented with 0.5% Triton X-100 and 4% milk. For animals that underwent the sensory deprivation procedure, some slices were incubated overnight with a mouse anti-tyrosine hydroxylase (TH) primary antibody (Immunostar, ref. 22941, 1:1000) to compare deprived and control OBs. TH labeling is commonly used to assess sensory deprivation efficiency, with occlusion resulting in a 50% decrease in the TH signal in the ipsilateral hemisphere[9]. The corresponding secondary antibodies were then used. Fluorescence images were acquired using an inverted Zeiss microscope (LSM 700, AxioObserver) with a 63X oil immersion objective (Plan Apochromat, NA: 1.4). To optimize image acquisition, we used a resolution of 1024 × 1024 pixels with pixels of size 0.05 µm × 0.05 µm and an optical sectioning of 0.35 µm. Confocal microscopy was chosen because it is a widely used technique to visualize spines. For reproducibility purposes and for the robustness of the analysis, the same imaging parameters were used for the entire study.

Dendritic and dendritic spine reconstructions

First, animals and experiments were anonymized to avoid any bias during extraction. Confocal images of GC spines collected from the different experimental groups were pre-processed with the DAMAS deconvolution algorithm[31,32] using the Iterative Deconvolve 3D plugin in ImageJ 1.53c[54]. The adapted DAMAS algorithm begins with a standard beamforming approach, utilizing the intensity of the pixels in the image. Then, in an iterative process, regions with the lowest intensity are progressively removed, and beamforming is recalculated at each step. This method leads to a robust deconvolution that enhances image clarity and detail. The images were then segmented using a Morphological Active Contours without Edges algorithm[34–36] with the convergence set at 100 iterations and the parameter µ set at 1, which influences the smoothing and depends on the complexity of the segmented object. The other two parameters, λ_1 and λ_2, were set at 1 and 9, respectively, as these parameters are related to the ratio between intensity and background. These parameters were determined empirically to increase the signal-to-noise ratio but were kept the same for all images. After segmentation, some images had visual artifacts in the form of single black pixels (value = 0) and were removed with a python script. In this script, for each black pixel, if the pixel was surrounded by at least 8 pixels with a value >0, the value of the black pixel was set as the mean of the surrounding pixels. The processed images were converted into meshes using the marching cubes algorithm[37,38]. The spacing used in the algorithm was 0.24, 0.05, 0.05, which corresponds to the pixel size for axes z, x, and y. The z axis was corrected for spherical aberration[55]. A polygonal mesh was generated using triangles to reproduce the surface of the spine. Each triangle was composed of vertices and was connected by edges. Before extracting the spines, a custom optimization process was performed using the following steps: a box was created around the mesh. Then, the target length was determined using the diagonal of this mesh box. Subsequently, a decision was made regarding the target level of detail, with 'normal' being the chosen setting. This was followed by the removal of degenerated triangles, specifically those that were collinear. The process also involved eliminating isolated vertices that were not connected to any face or edge. Then, the removal of self-intersecting edges and faces, as well as the elimination of duplicated faces. Isolated vertices were then removed a second time. To ensure there were no reconstruction issues with the mesh, the outer hull volume was calculated. The process continued with the removal of obtuse triangles, those with an angle greater than 179 degrees. Another round of removing duplicated faces and vertices was conducted. Finally, the integrity of the mesh was assessed. In cases where the mesh was found to be broken, the entire process was restarted from the third step, albeit using a lower level of detail.

After this reconstruction, the spines were extracted manually from the dendrite using Meshlab software[56].

Measurement of morphometric features

To measure the morphometric features of the reconstructed spines, the hole left from the separation of the spine from the dendrite was used to calculate the position of the spine base center (S_{bc}). Graph theory was used to assess the number of neighbors of each vertex. Because the vertices with the lowest number of neighbors were closest to the spine base with only three neighbors, the spine base center can be defined as the mean coordinate of these vertices.

Length (L). The Length between each vertex (N) of the mesh in three dimensions (x, y, z) and the spine base center (S_{bc}) is first calculated:

$$\vec{l_i} = \left(x_i - S_{bc_x}, y_i - S_{bc_y}, z_i - S_{bc_z}\right)$$

Then, a new mathematical subset is defined with the 5% longest distance (n). The final length is determined as the mean of these lengths:

$$L = 1/n \sum_{i=1}^{n} l_i$$

Surface (S). The spine Surface area is the sum of all the triangle surfaces (s):

$$S = \sum_{i=1}^{f} s_i$$

A triangle surface (s) is defined for every face (f) of the spine. For each triangle (i) with summits A, B, and C:

$$s_i = \frac{1}{2}\left|\overrightarrow{AB} \times \overrightarrow{AC}\right|$$

Volume (V). The spine Volume is the sum of the entire tetrahedron volume (v):

$$V = \sum_{i=1}^{f} v_i$$

Each tetrahedron is defined by 4 vertices corresponding to triangles A, B, and C, and the spine center (S_C) for all three-space coordinates (x, y, z). The tetrahedron volume is then calculated:

$$v_i = \frac{1}{6}\left(\overrightarrow{AB} \times \overrightarrow{AC}\right) \cdot AS_c$$

Hull Volume (HV). The Hull Volume represents the smallest convex set containing all the vertices of a geometric shape. The calculation of the Hull Volume is performed using the built-in function of the Python package trimesh 3.7.10, which is based on the Quickhull algorithm[57].

Hull Ratio (HR). The Hull Ratio is determined as:

$$HR = \frac{HV - V}{V}$$

It can represent the complexity of the structure. The higher the score, the more complex the mesh.

Average Distance (AD). The Average Distance represents the mean distance between each vertex (N) and the spine base center.

$$AD = \frac{1}{N}\sum_{i=1}^{N}\left(\left|\vec{l}_i\right|\right)$$

Coefficient of Variation in Distance (CVD). The Coefficient of Variation in Distance represents the standard deviation of the variation of distance between the base of the spines and each vertex.

$$CVD = \frac{\sqrt{\frac{\sum_{i=1}^{N}|l_i - \mu|^2}{N}}}{AD}$$

A high CVD is correlated with a large variation between the distance of the spine base center and the vertices. A high CVD often leads to mushroom-like spines while a small CVD leads to small stubby or small thin spines.

Open Angle (OA). The Open Angle corresponds to the average angle between the spine axis and each vertex vector. The spine axis was defined as the vector crossing the gravity center (G_c) and the mesh base center (S_{bc}). The vertex vector is defined as the vector (l_i) crossing the vertex and the mesh base center.

$$OA = \frac{1}{N}\sum_{i=1}^{N}\cos^{-1}\left(\overrightarrow{G_cS_{bc}} \cdot \overrightarrow{l_iS_{bc}}\right)$$

Large head spines are associated with a higher OA value, and thin spines with a low OA value.

Mean Curvature (MC). The Mean Curvature corresponds to the mean of the curvature of each face of the mesh. It was calculated using trimesh[58] and was then normalized to the surface.

$$MC = \sum_{i=1}^{N}\frac{mc_i}{A_i}$$

Mean Gaussian Curvature (GC). The Mean Gaussian Curvature corresponds to the mean of the gaussian curvature of each face of the mesh. The main difference between GC and MC is that GC is quadratic while MC is linear. It was calculated using trimesh based on[58] and was then normalized to the surface.

Dimension reduction, clustering, and statistical analysis

The correlation matrix was calculated, and a PCA was performed using the Python package scikit-learn 1.0.2. A clustering analysis without implementing PCA on the five features was performed. For this analysis, we computed the same three different scores: Silhouette, Elbow, and Calinski-Harabasz to determine the optimal number of clusters. Notably, these scores yielded differing recommendations regarding the number of clusters. We hypothesize that the observed variance in cluster strength may be due to the lack of dimension reduction in this particular analysis. Without the application of PCA, metrics of lower significance potentially gain more influence, and as a result, the impact of noise within the dataset is likely to be more pronounced. This exploratory test highlights the value of dimension reduction techniques like PCA in enhancing the robustness of clustering analyses. We used PCA to reduce the number of features from five to three independent components. Altogether, these three Principal Components (PC) contained 85.4% of the variance in the dataset. The clustering was performed using the K-Means algorithm[59] included in scikit-learn 1.0.2. The number of clusters was determined and was validated using three different scores: the Calinski-Harabz score[60], the Silhouette score[61], and the Elbow score[62]. After clustering, the significance between the percentage of each cluster was determined using a two-independent proportion Agresti-Caffo test, which is available in statsmodels[63]. $P < 0.05$ are considered statistically significant ($^*p < 0.05$, $^{**}p < 0.01$, $^{***}p < 0.001$). The Python package seaborn 0.12.1dev0 was used to generate the KDE maps. The Python package pingouin 0.5.3 was used to calculate Cohen's term d. An effect lower than 0.01 is considered very small while an effect lower than 0.20 is considered small. To evaluate the potential lack of independence and variability between groups in the data, particularly considering that many spines share the same cell and animal, the Intracluster Correlation Coefficient (ICC) was employed. This was calculated using pingouin version 0.5.3. For the spine density of the simple go/no experiment, the ICC is 0.8399. For the spine density of the complex go/no experiment, the ICC is 0.8275. Finally, for the spine density of the sensory deprivation experiment, the ICC is 0.8967. Since these coefficients are above 0.75, these results demonstrate that inter-cell/mouse variability is not significant in the dataset[64].

Reporting summary

Further information on research design is available in the Nature Portfolio Reporting Summary linked to this article.

Data availability

The source data for the graphs in the paper can be found in Supplementary Data 1. Further information and requests for resources and reagents should be directed to and will be fulfilled by the co-corresponding authors, Dr. Armen Saghatelyan (asaghate@uottawa.ca) and Dr. Simon V. Hardy (simon.hardy@ift.ulaval.ca).

Code availability

Codes for the reconstruction and the analysis[65] are available at https://zenodo.org/records/10622371.

Received: 27 July 2023; Accepted: 27 March 2024;
Published online: 06 April 2024

References

1. Erzurumlu, R. S. & Gaspar, P. Development and critical period plasticity of the barrel cortex. *Eur. J. Neurosci.* **35**, 1540–1553 (2012).
2. Malvaut, S. & Saghatelyan, A. The role of adult-born neurons in the constantly changing olfactory bulb network. *Neural Plast.* **2016**, 1614329 (2016).
3. Denoth-Lippuner, A. & Jessberger, S. Formation and integration of new neurons in the adult hippocampus. *Nat. Rev. Neurosci.* **22**, 223–236 (2021).
4. Hardy, D. & Saghatelyan, A. Different forms of structural plasticity in the adult olfactory bulb. *Neurogenesis* **4**, e1301850 (2017).
5. Sailor, K. A. et al. Persistent structural plasticity optimizes sensory information processing in the olfactory bulb. *Neuron* **91**, 384–396 (2016).
6. Wu, Z. et al. Context-dependent decision making in a premotor circuit. *Neuron* **106**, 316–328. e6 (2020).
7. Lepousez, G. et al. Olfactory learning promotes input-specific synaptic plasticity in adult-born neurons. *Proc. Natl Acad. Sci.* **111**, 13984–13989 (2014).
8. Lledo, P.-M. & Saghatelyan, A. Integrating new neurons into the adult olfactory bulb: joining the network, life–death decisions, and the effects of sensory experience. *Trends Neurosci.* **28**, 248–254 (2005).
9. Bastien-Dionne, P. O. et al. Role of sensory activity on chemospecific populations of interneurons in the adult olfactory bulb. *J. Comp. Neurol.* **518**, 1847–1861 (2010).
10. Kelsch, W. et al. A critical period for activity-dependent synaptic development during olfactory bulb adult neurogenesis. *J. Neurosci.* **29**, 11852–11858 (2009).
11. Breton-Provencher, V. et al. Principal cell activity induces spine relocation of adult-born interneurons in the olfactory bulb. *Nat. Commun.* **7**, 12659 (2016).
12. Malvaut, S. et al. CaMKIIα expression defines two functionally distinct populations of granule cells involved in different types of odor behavior. *Curr. Biol.* **27**, 3315–3329. e6 (2017).
13. Belnoue, L. et al. A critical time window for the recruitment of bulbar newborn neurons by olfactory discrimination learning. *J. Neurosci.* **31**, 1010–1016 (2011).
14. Magavi, S. S. et al. Adult-born and preexisting olfactory granule neurons undergo distinct experience-dependent modifications of their olfactory responses in vivo. *J. Neurosci.* **25**, 10729–10739 (2005).
15. Malvaut, S. & Saghatelyan, A. Regeneration in the olfactory bulb. In *the senses: A Comprehensive Reference* (ed. Fritzsch, B.) 610–623 (Academic Press, 2020).
16. Alonso, M. et al. Activation of adult-born neurons facilitates learning and memory. *Nat. Neurosci.* **15**, 897–904 (2012).
17. Li, W. L. et al. Adult-born neurons facilitate olfactory bulb pattern separation during task engagement. *Elife* **7**, e33006 (2018).
18. Grelat, A. et al. Adult-born neurons boost odor-reward association. *Proc. Natl Acad. Sci. USA* **115**, 2514–2519 (2018).
19. Kharazia, V. N. & Weinberg, R. J. Immunogold localization of AMPA and NMDA receptors in somatic sensory cortex of albino rat. *J. Comp. Neurol.* **412**, 292–302 (1999).
20. Takumi, Y. et al. Different modes of expression of AMPA and NMDA receptors in hippocampal synapses. *Nat. Neurosci.* **2**, 618–624 (1999).
21. Ganeshina, O. et al. Differences in the expression of AMPA and NMDA receptors between axospinous perforated and nonperforated synapses are related to the configuration and size of postsynaptic densities. *J. Comp. Neurol.* **468**, 86–95 (2004).
22. Arellano, J. I., et al., Ultrastructure of dendritic spines: correlation between synaptic and spine morphologies. *Front. Neurosci*. **1**,131–143 (2007).
23. Tønnesen, J. et al. Spine neck plasticity regulates compartmentalization of synapses. *Nat. Neurosci.* **17**, 678–685 (2014).
24. Rodriguez, A. et al. Automated three-dimensional detection and shape classification of dendritic spines from fluorescence microscopy images. *PloS One* **3**, e1997 (2008).
25. Ghani, M. U. et al. Dendritic spine classification using shape and appearance features based on two-photon microscopy. *J. Neurosci. Methods* **279**, 13–21 (2017).
26. Bokota, G. et al. Computational approach to dendritic spine taxonomy and shape transition analysis. *Front. Comput. Neurosci.* **10**, 140 (2016).
27. Pchitskaya, E. & Bezprozvanny, I. Dendritic spines shape analysis—classification or clusterization? Perspective. *Front. Synaptic Neurosci.* **12**, 31 (2020).
28. Ghani, M. U., et al. Dendritic spine shape analysis: a clustering perspective. In *Proc. Computer Vision–ECCV 2016 Workshops: Amsterdam, The Netherlands, October 8–10 and 15–16, 2016, Proceedings, Part I 14* (Springer, 2016).
29. Ekaterina, P. et al. SpineTool is an open-source software for analysis of morphology of dendritic spines. *Sci. Rep.* **13**, 10561 (2023).
30. Zuo, Y. et al. Long-term sensory deprivation prevents dendritic spine loss in primary somatosensory cortex. *Nature* **436**, 261–265 (2005).
31. Brooks, T. F. & Humphreys, W. M. A deconvolution approach for the mapping of acoustic sources (DAMAS) determined from phased microphone arrays. *J. Sound Vib.* **294**, 856–879 (2006).
32. Dougherty, R. Extensions of DAMAS and benefits and limitations of deconvolution in beamforming. In *Proc. 11th AIAA/CEAS Aeroacoustics Conference* (AIAA, 2005).
33. Viola, P. and W. M. Wells. Alignment by maximization of mutual information. In *Proc. IEEE International Conference on Computer Vision* (IEEE, 1995).
34. Alvarez, L., et al. Morphological snakes. In *Proc. 2010 IEEE Computer Society Conference on Computer Vision and Pattern Recognition* (IEEE, 2010).
35. Chan, T. F. & Vese, L. A. Active contours without edges. *IEEE Trans. Image Process.* **10**, 266–277 (2001).
36. Marquez-Neila, P., Baumela, L. & Alvarez, L. A morphological approach to curvature-based evolution of curves and surfaces. *IEEE Trans. Pattern Anal. Mach. Intell.* **36**, 2–17 (2013).
37. Lewiner, T. et al. Efficient implementation of marching cubes' cases with topological guarantees. *J. Graph. Tools* **8**, 1–15 (2003).
38. Lorensen, W. E. & Cline, H. E. Marching cubes: a high resolution 3D surface construction algorithm. *ACM SIGGRAPH Comput. Graph.* **21**, 163–169 (1987).
39. Schober, P., Boer, C. & Schwarte, L. A. Correlation coefficients: appropriate use and interpretation. *Anesth. Analg.* **126**, 1763–1768 (2018).
40. Yuste, R. & Bonhoeffer, T. Genesis of dendritic spines: insights from ultrastructural and imaging studies. *Nat. Rev. Neurosci.* **5**, 24–34 (2004).
41. Lagier, S., Carleton, A. & Lledo, P.-M. Interplay between local GABAergic interneurons and relay neurons generates γ oscillations in the rat olfactory bulb. *J. Neurosci.* **24**, 4382–4392 (2004).
42. Fukunaga, I. et al. Independent control of gamma and theta activity by distinct interneuron networks in the olfactory bulb. *Nat. Neurosci.* **17**, 1208–1216 (2014).
43. Sailor, K. A., Schinder, A. F. & Lledo, P.-M. Adult neurogenesis beyond the niche: its potential for driving brain plasticity. *Curr. Opin. Neurobiol.* **42**, 111–117 (2017).

44. Lledo, P.-M., Alonso, M. & Grubb, M. S. Adult neurogenesis and functional plasticity in neuronal circuits. *Nat. Rev. Neurosci.* **7**, 179 (2006).
45. Forest, J. et al. Short-term availability of adult-born neurons for memory encoding. *Nat. Commun.* **10**, 5609 (2019).
46. Saghatelyan, A. et al. Activity-dependent adjustments of the inhibitory network in the olfactory bulb following early postnatal deprivation. *Neuron* **46**, 103–116 (2005).
47. Mandairon, N. et al. Involvement of newborn neurons in olfactory associative learning? The operant or non-operant component of the task makes all the difference. *J. Neurosci.* **31**, 12455–12460 (2011).
48. Tronel, S. & Sara, S. J. Mapping of olfactory memory circuits: region-specific c-fos activation after odor-reward associative learning or after its retrieval. *Learn. Mem.* **9**, 105–111 (2002).
49. Luengo-Sanchez, S. et al. 3D morphology-based clustering and simulation of human pyramidal cell dendritic spines. *PLoS Comput. Biol.* **14**, e1006221 (2018).
50. Batista-Brito, R. et al. The distinct temporal origins of olfactory bulb interneuron subtypes. *J. Neurosci.* **28**, 3966–3975 (2008).
51. Hardy, D. et al. The role of calretinin-expressing granule cells in olfactory bulb functions and odor behavior. *Sci. Rep.* **8**, 9385 (2018).
52. Kucharski, D. & Hall, W. New routes to early memories. *Science* **238**, 786–788 (1987).
53. Cummings, D., Henning, H. & Brunjes, P. Olfactory bulb recovery after early sensory deprivation. *J. Neurosci.* **17**, 7433–7440 (1997).
54. Schneider, C. A., Rasband, W. S. & Eliceiri, K. W. NIH Image to ImageJ: 25 years of image analysis. *Nat. methods* **9**, 671–675 (2012).
55. Kashiwagi, Y. et al. Computational geometry analysis of dendritic spines by structured illumination microscopy. *Nat. Commun.* **10**, 1285 (2019).
56. Cignoni, P. et al. Meshlab: an open-source mesh processing tool. In *Proc. Eurographics Italian Chapter Conference* 129–136 (Eurographics Association, 2008).
57. Barber, C. B., Dobkin, D. P. & Huhdanpaa, H. The quickhull algorithm for convex hulls. *ACM Trans. Math. Softw. (TOMS)* **22**, 469–483 (1996).
58. Cohen-Steiner, D. & Morvan, J.-M. Restricted delaunay triangulations and normal cycle. In *Proc. Nineteenth Annual Symposium on Computational Geometry* 312–321 (Association for Computing Machinery, 2003).
59. Arthur, D. & Vassilvitskii, S. *k-means++: The advantages of careful seeding* (Stanford, 2006).
60. Caliński, T. & Harabasz, J. A dendrite method for cluster analysis. *Commun. Stat.-Theory Methods* **3**, 1–27 (1974).
61. Rousseeuw, P. J. Silhouettes: a graphical aid to the interpretation and validation of cluster analysis. *J. Comput. Appl. Math.* **20**, 53–65 (1987).
62. Yuan, C. & Yang, H. Research on K-value selection method of K-means clustering algorithm. *J* **2**, 226–235 (2019).
63. Agresti, A. & Caffo, B. Simple and effective confidence intervals for proportions and differences of proportions result from adding two successes and two failures. *Am. Statistician* **54**, 280–288 (2012).
64. Aarts, E. et al. A solution to dependency: using multilevel analysis to accommodate nested data. *Nat. Neurosci.* **17**, 491–496 (2014).
65. Ferreira, A., et al. Spine reconstruction and analysis pipeline for Distinct forms of structural plasticity of adult-born mouse interneuron spines induced by different odor learning paradigms. Zenodo. https://doi.org/10.5281/zenodo.10622371(2024)

Acknowledgements

This work was supported by a Canadian Institute of Health Research (CIHR) grant to A.S., National Science and Engineering Research Council of Canada (NSERC) grants to S.V.H. and A.S., and a Le Fonds de recherche du Québec—Nature et technologies (FRQNT) team grant to A.S. and S.V.H.

Author contributions

A.F. performed the computational analyses of the spines of adult-born neurons. V.S.C. and S.M. performed the experiments and acquired the images. S.V.H. and A.S. supervised the computational and experimental work, respectively. All the authors discussed the data, and A.F., S.M., A.S., and S.V.H. wrote the manuscript.

Competing interests

The authors declare no competing interests.

Additional information

Supplementary information The online version contains supplementary material available at https://doi.org/10.1038/s42003-024-06115-7.

Correspondence and requests for materials should be addressed to Armen Saghatelyan or Simon V. Hardy.

Peer review information *Communications Biology* thanks Matthew Grubb, Ali Ozgur Argunsah, and Andreas (M) Kist for their contribution to the peer review of this work. Primary Handling Editors: George Inglis and Benjamin Bessieres.